scientific reports

Check for updates

OPEN

Synthesis, nanocrystalline morphology, lattice dynamics and nonlinear optics of mesoporous SiO_2&$LiNbO_3$ nanocomposite

Yaroslav Shchur[1]✉, Houda El Karout[2,3], Bouchta Sahraoui[3], Anatoliy Andrushchak[4], Guillermo Beltramo[5], Denys Pustovyi[6], Svetlana Vitusevich[6], Patrick Huber[7,8] & Andriy V. Kityk[9]

We demonstrate a hybrid nanocomposite combining mesoporous silica, *p*SiO_2, as a host medium and guest lithium niobate $LiNbO_3$ nanocrystals embedded into tubular silica nanochannels by calcination of the precursor mixed solution of lithium and niobium salts. High-resolution transmission electron microscopy, X-ray diffraction and Raman scattering techniques reveal trigonal $LiNbO_3$ nanocrystals within the *p*SiO_2 nanochannels, indicating their random texture morphology. Annealing at high temperatures (950°C) during calcination also leads to partial crystallization of the *p*SiO_2 matrix with the formation of trigonal α-SiO_2 nanocrystals. The Raman microscopy analysis of the *p*SiO_2:$LiNbO_3$ nanocomposite reveals three structural crystalline phases, $\alpha - SiO_2$, $LiNbO_3$ and a mixed phase which involves the α-SiO_2 phase of host membrane and $LiNbO_3$ nanocrystals embedded into the membrane. The finite size of the $LiNbO_3$ nanocrystals results in specific features of the LO-TO phonon frequency splitting, which are investigated by Raman microscopy. In the transmission geometry, the second harmonic generation emission exhibits no Maker fringes and is characterized by a broad angular diagram of diffusely scattered light. The second harmonic generation response is independent of the polarization direction of the incident pump light, thus indicating a spatial isotropy of the nonlinear optical conversion in the *p*SiO_2:$LiNbO_3$ composite, consistent with the randomly oriented textural morphology of the deposited $LiNbO_3$ nanocrystals. The contribution of the guest $LiNbO_3$ nanocrystals to the second harmonic generation effect was found to be strongly dominant compared to the partially crystallized host *p*SiO_2 matrix. The nanocomposite *p*SiO_2:$LiNbO_3$ membrane, set in the 90° nonlinear optical geometry, shows unusually high diffusely transmitted second harmonic generation light (back-reflected emission), apparently supported by internal light reflection from the tubular nanochannel network. Despite the fundamental interest, the revealed anomalous back-reflected second harmonic generation emission from *p*SiO_2:$LiNbO_3$ nanocomposite membranes expands the prospects for their photonic and nonlinear optical applications.

The design of hybrid nanocomposites represents a powerful synthetic approach that allows tuning and tailoring the optical and electronic properties of resultant composite materials in a desired manner, thus enabling their targeted applicability for advanced optoelectronic, nonlinear optical (NLO) and photonic applications[1–13]. Nanoporous silica, (*p*SiO_2, hereafter *PS*), represents a good hosting material for hybrid composite technologies. Obtained by the oxidation of mesoporous silicon (*p*Si)[14], mesoporous silica *PS*[15] retains its tubular morphology resulting from the electrochemical etching procedure. Due to this feature, amorphous *PS* membranes exhibit

[1]Institute for Condensed Matter Physics, 1 Svientsitskii str, 79011 Lviv, Ukraine. [2]University of Angers, MOLTECH, Anjou-UMR CNRS, SFR MATRIX, Angers Cedex 01, 6200, 49000 Angers, France. [3]University of Angers, LPhIA, SFR MATRIX, 2 Bd. Lavoisier, Cedex 01, 49045 Angers, France. [4]Lviv National Polytechnic University, 12 S. Bandery str., 79013 Lviv, Ukraine. [5]Institute of Biological Information Processing Mechanobiology (IBI-2), Forschungszentrum Jülich, D-52425 Jülich, Germany. [6]Institute of Bioelectronics (IBI-3), Forschungszentrum Jülich, D-52425 Jülich, Germany. [7]Institute for Materials and X-ray Physics, Hamburg University of Technology, Denicke Str. 15, 21073 Hamburg, Germany. [8]Centre for X-ray and Nano Science CXNS, Deutsches Elektronen-Synchrotron DESY, Notkestr. 85, 22605 Hamburg, Germany. [9]Faculty of Electrical Engineering, Częstochowa University of Technology, Al. Armii Krajowej 17, 42-200 Częstochowa, Poland. ✉email: shchur@icmp.lviv.ua

dielectric and optical anisotropy that can be tuned by combining them with suitable liquid, soft, or solid guest materials, such as e.g. liquid crystals[6,10,11,16,17], amorphous organic compounds[7] and a wide range of inorganic[18,19] or organic[8,20] crystalline materials. In such a hybrid nanocomposite technology, a scaffold amorphous structure of *PS* matrix provides mechanical robustness, while the deposited guest material with specific physical and chemical properties ensures relevant functionality of the resulting composite material. A prominent example is the recently demonstrated silica-benzil nanocomposites[8,20], in which a second-order optical nonlinearity originates from non-centrosymmetric organic nanocrystals embedded in cylindrical nanochannels of an optically inactive *PS* matrix. Spatial confinement and interfacial interactions were found to be crucial here significantly influencing both the textural morphology of organic guest crystals and the associated NLO performance along with its anisotropy, explored particularly in second harmonic generation (SHG) experiments. It turned out that the embedded benzil nanoclusters are not uniformly crystalline but are characterized by a more complex morphology consisting of a disordered SHG-inactive amorphous shell and a SHG-active crystalline core[8]. The SHG response vanishes when spatial cylindrical confinement approaches the sizes of a few molecular layers.

Inorganic nanocrystals as a guest composite component can be considered as a robust alternative approach in the technology of advanced optical and photonic materials. Indeed, many inorganic crystalline materials are characterized by large NLO constants. Additionally, their main advantages are a wide window of optical transparency and a high optical damage threshold compared to their organic counterparts, as demonstrated by a number of inorganic crystalline materials. Lithium niobate ($LiNbO_3$ or *LNO*) is a prominent example, the most versatile and widely used crystalline optical material. A large number of acousto-electronic and optoelectronics applications are based on this material which exhibits unique piezoelectric[21–24], birefringent[25–27], photorefractive[28,29], electrooptic[30–32], photoelastic[33] and NLO[34–38] properties combined with excellent mechanical and chemical stability and wide optical transparency in the UV-Vis-IR spectral region ($320 \leq \lambda \leq 3400$ nm[39,40]). Large electro-optic constants of *LNO* crystals make them applicable in electro-optical devices, such as e.g. Pockels cells for light modulation[43,44] and laser Q-switches[41,42]. Thin-film *LNO* emerges as a promising platform for photonic integrated circuits, particularly as high-speed electro-optic modulators[45]. Pure and especially metal-doped *LNO* crystals, due to their high photorefractivity, serve as efficient and high-capacity holographic storage materials[46]. Considerable second-order optical nonlinearity, on the other hand, allows to successfully use this crystalline material for laser frequency upconversion, i.e., the SHG or sum-frequency generation[47], as well as spontaneous parametric down-conversion[48] to produce frequency-tunable coherent emission. Relevant functionalities may be added to an amorphous *PS*-matrix which itself is macroscopically centrosymmetric, and the corresponding effects are symmetry forbidden.

In the present work we demonstrate silica-lithium niobate, $p SiO_2$:$LiNbO_3$ (hereafter *PS*:*LNO*) nanocomposites. A significant challenge in the fabrication of such hybrid materials is the deposition of *LNO* nanocrystals in a tubular *PS* network. *LNO* is characterized by a high melting point (T_m=1253^{o}C[49]), which makes the capillary melt imbibition technique, usually used in the synthesis of organic-inorganic nanocomposites, inapplicable. Grigas and Kaskel[50] have offered a breakthrough synthesis approach starting from a precursor mixture solution of lithium and niobium salts with its subsequent calcination in nanochannels of mesoporous silica powder SBA-15. However, SBA-15:*LNO* nanocomposites obtained in such a way are characterized by micro-powder morphology which evidently limits their optical application. Therefore, the synthesis of monolithic samples of centimeter size remains a priority. For this reason, the synthesis methodology developed in[50] has been applied by using mesoporous *PS* membranes, synthesized by oxidation of electrochemically etched silicon, as host composite media. The *PS* nanochannels play the role of tubular nanoreactors that stabilize the nanoparticles against sintering while the heat treatment promotes crystallization.

X-ray diffraction (XRD) is used here to evidence *LNO* nanocrystals inside nanochannels and characterize their textural morphology, whereas high-resolution transmission electron microscopy (HRTEM) provides direct imaging of the atomic structure of *LNO* nanocrystals embedded into *PS*-matrix. Raman microscopy, on the other hand, in combination with the group-theory analysis represents powerful tools in the exploration of lattice dynamics of *LNO* nanocrystals whereas comparison of *PS*:*LNO* Raman spectra with bulk *LNO* allows to conclude about the influence of spatial nanoconfinement on it. The SHG experiments aim to explore the second order NLO properties of *PS*:*LNO* composites. Due to the specific features of *PS*:*LNO* membranes, namely their large diffuse light scattering, the NLO properties are investigated using both transmission and reflection geometry.

Results and discussion

Synthesis of PS:LNO nanocomposites

.

The *PS*:*LNO* composites were prepared in several consequent steps (see Figure 1). In the first step, the porous silicon *p*Si-membranes were obtained by electrochemical anodic etching (∼8 hours) of highly *p*-doped $\langle 100 \rangle$ -oriented silicon wafers (resistivity of 0.01 Ω·cm)) using an electrolyte mixture of HF:C_2H_5OH (2:3) and a DC current density of 12 mA/cm^2[51]. The formed mesoporous layer was released from the underlying Si-wafer by a sudden increase in the etching current by about one order of magnitude at the end of the etching process. In the second step, the free-standing *p*Si membranes were thermally oxidized for 12 hours at T=800^{o}C under standard atmosphere. The synthesized flow-through (double-sided open) mesoporous silica membranes had a porosity of 46±2% and a thickness of about 250±5 μm. The average channel diameter of the synthesized PS membranes equals 12.0±1.0 nm as verified from volumetric N_2-sorption isotherm recorded at T = 77 K.

PS-membranes, annealed thermally at 180^{o}C, were cooled down to the temperature of about 60^{o}C and using a spontaneous capillary imbibition were filled with the precursor solution prepared in accordance with[50], i.e., nearly saturated equimolar aqueous solution of $LiNO_3$ (99.999%, Alfa Aesar) and $NH_4NbO(C_2O_4)_2 \cdot xH_2O$ (99.99%, Sigma Aldrich). The filled *PS*-membranes were dried for ∼15 min and then twice refilled with precursor

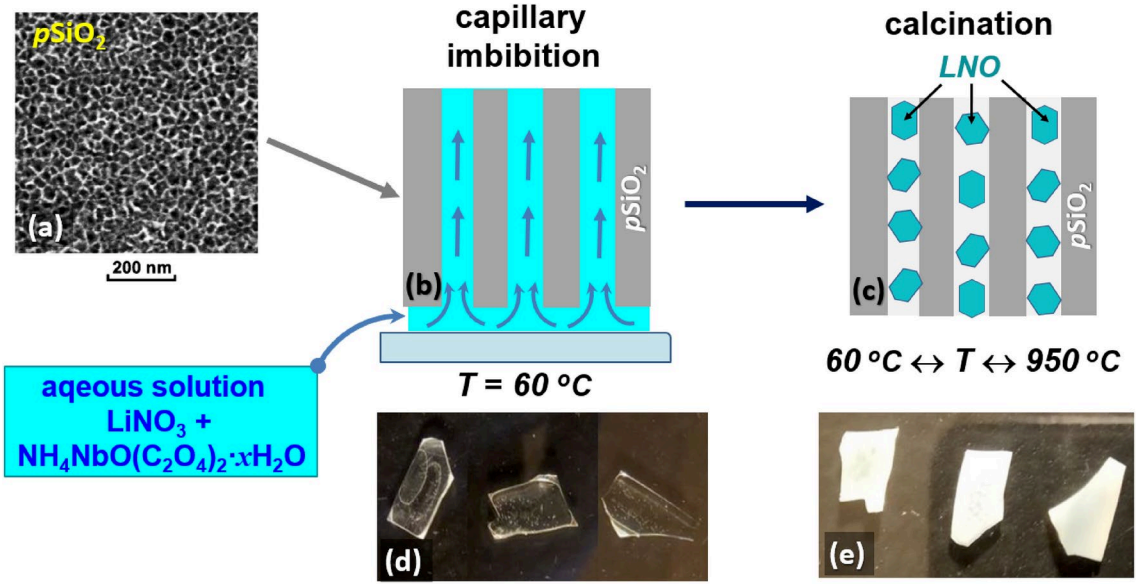

Fig. 1. Synthesis of *PS:LNO* nanocomposites. Mesoporous silica ($p\mathrm{SiO}_2$, PS) membranes (a), obtained by oxidation of electrochemically etched mesoporous silicon (SEM image, Sec.(a)), constitute the host matrix in the composite synthesis, whereas nearly saturated equimolar aqueous solution of LiNO_3 and $\mathrm{NH}_4\mathrm{NbO}(\mathrm{C}_2\mathrm{O}_4)_2{\cdot}x\mathrm{H}_2\mathrm{O}$ represents precursor solution. The *PS* nanochannels were filled by spontaneous capillary imbibition with the precursor solution (Sec.(b)). Calcination of precursor content in the regime of slow heating to a temperature of 950^{o}C leads to the formation of randomly oriented *LNO* nanocrystals inside the silica nanochannels (Sec.(c)). Sec.(d) and (e) show several composite samples before and after their calcination, respectively. The white, opaque color of calcined *PS:LNO* nanocomposite samples results from the large diffusive light scattering by the deposited *LNO* nanocrystals, which is typical of dispersively filled mesoporous *PS* substrates.

solution to reach a larger amount of precursor salt components deposited in the nanochannels. The calcination of the precursor content and its subsequent crystallization to *LNO* was carried out in air by placing impregnated *PS*-membranes in a furnace operated in the regime of heating ramp (∼3 - 5 ^{o}C/min) up to the temperature of 950^{o}C and then cooling down to room temperature. The empty silica membranes were optically transparent, as shown in the photograph in Figure 1,(d). Therefore, the *LNO* nanocrystals randomly distributed in the silica nanochannels seem to be the only morphological factor determining the opacity of the *PS:LNO* composite, as shown in Fig. 1e. The volume fraction of *LNO* nanocrystals inside the nanochannels, approximately estimated from the initial chemical reagents, is in the range of 8±2%.

Textural morphology of *PS:LNO* nanocomposites: X-ray diffraction and high-resolution transmission electron microscopy

.

XRD techniques (DRON-3, $\mathrm{Cu\text{-}K}_\alpha$ radiation) was utilized for the characterization of the calcined crystal phases. Figure 2 shows conventional $\theta/2\theta$ reflection XRD geometry (insert) along with the XRD patterns recorded from both sides of the nanocomposite *PS:LNO*. The reference patterns of bulk trigonal *LNO* and $\alpha-\mathrm{SiO}_2$ crystals are presented for comparison. The XRD patterns were recorded at room temperature in the 10° to 70° angular range with a step of 0.01° and scan rate of 3°/min. As compared to JCPDS (card No. 020-0631), the Bragg reflections that appeared at 23.75°, 32.75°, 34.87°, 48.58°, 53.29°, 61.16° and 62.50°, see indexed XRD peaks marked with arrows (green color online), correspond to the trigonal *LNO* phase. The remaining peaks at 20.89°, 36.56°, 50.16° and 59.96°, see indexed XRD peaks marked with arrows (gray color online), indicate the presence of the trigonal crystal $\alpha-\mathrm{SiO}_2$ phase (JCPDS card No. 33-1161), apparently due to partial crystallization of the amorphous silica matrix as a side effect of composite calcination at high temperatures. The ratios between the intensities of Bragg peaks are similar to that given in the relevant reference powder XRD patterns. Accordingly, one may conclude that both *LNO* and $\alpha-\mathrm{SiO}_2$ nanocrystallites are oriented in *PS:LNO* composite almost randomly, i.e., one deals with a very weak texture, if any. By extracting the full widths at half maximum (FWHM) of XRD peaks and applying the Scherrer equation[53], one obtains the size of the embedded *LNO* crystallites of about 22-23 nm along nanochannels, i.e., perpendicular to the silica membrane faces, whereas relevant evaluations for $\alpha-\mathrm{SiO}_2$ phase give only a bit larger crystallite size, about 24-25 nm.

The HRTEM techniques provides a direct imaging of the nanocrystalline particle embedded into the *PS* matrix. The ultrathin lamella with the surface of 5×15 μm^2 and thickness of around 70 nm has been prepared using a helium focused ion beam. The initial sample was covered with a 50 nm thick gold layer to prevent the electron scattering while depositing a protective 3μm-carbon layer on the surface. Such a carbon layer protected the lamella from destruction by ions during its fabrication. An ion beam (30kV, 6.5nA) was then used to carve

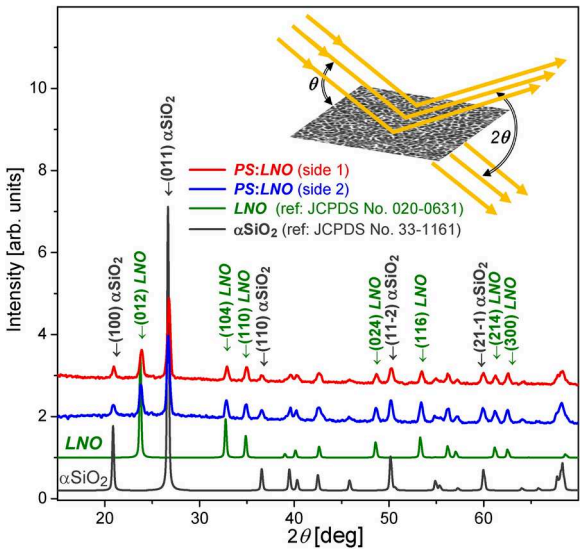

Fig. 2. Background subtracted XRD patterns ($\theta/2\theta$-scans) recorded from the opposite sides of nanocomposite *PS:LNO* membranes (blue and red online colors). The reference XRD powder patterns of *LNO* (JCPDS card No. 020-0631), green online color) and $\alpha - SiO_2$ (JCPDS card No. 33-1161, gray online color) are shown for comparison. The insert describes the XRD geometry used in the characterization of textural morphology in nanocomposite *PS:LNO* membranes.

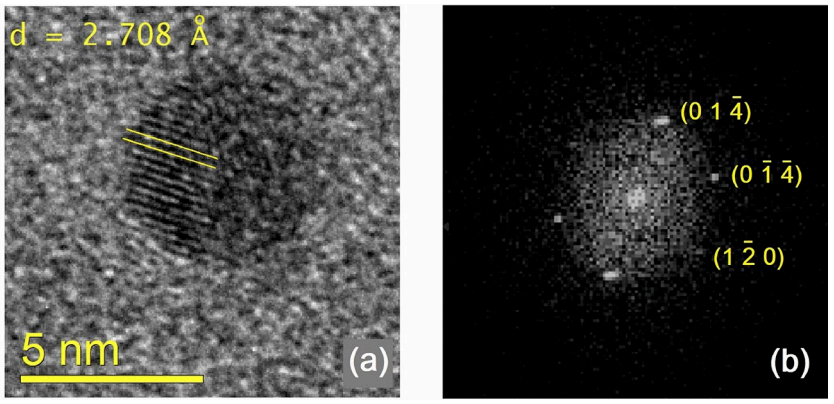

Fig. 3. Sec.(a): HRTEM of *PS:LNO* hybrid nanocomposite structure: An *LNO* nanocrystal embedded into the *PS*-matrix. The lattice spacing of d =2.708 Å corresponds to atomic planes identified by unique Miller indices (0 1 $\bar{4}$). Sec.(b): The FFT of the image presented in Sec.(a): The FFT spots correspond to atomic planes of *LNO* lattice identified by the unique Miller indices (0 1 $\bar{4}$), (0 $\bar{1}$ $\bar{4}$) and (1 $\bar{2}$ 0), see labels.

the lamella from the bulk sample. In the final stage, the carved lamella was attached to the lamella-holder, and fine etching with very low beam energy (5 kV, 47 pA) was used to polish the lamella, i.e., to reach its appropriate thickness suitable for further HRTEM study. From the HRTEM images taken from different places of the lamella, it can be concluded that the diameter of the pores ranges from ∼5 to ∼35 nm. The HRTEM image of the nanocrystalline particle embedded in smallest void of the silica matrix is shown in Fig. 3,(a). It manifests a round morphology, ∼5 nm in diameter, with a regular crystal structure characterized by the lattice spacing of d =2.708 Å which is close to $d_{01\bar{4}}$ =2.735 Å lattice spacing determined for the trigonal crystal system ($d_{hkl} = [(4(h^2 + hk + l^2)/(3a^2) + l^2/c^2]^{-1/2}$) with the lattice parameters for *LNO*a =5.14739 Å and c =13.85614 Å taken from Ref.[52]. The HRTEM technique allows, in particular, to distinguish the observed *LNO* nanocrystals from $\alpha - SiO_2$ crystallites, because the latter ones are characterized by much different lattice spacing values. The fast Fourier transform (FFT) of the image presented in Fig. 3,(a), provides the representation of the observed periodical crystal structure in the reciprocal space, see Fig. 3,(b). The FFT spots correspond to the atomic planes of *LNO* lattice identified by unique Miller indices (0 1 $\bar{4}$), (0 $\bar{1}$ $\bar{4}$) and (1 $\bar{2}$ 0), as labeled here.

Raman microscopy analysis

Micro-Raman analysis was performed at room temperature in back-scattering geometry using two Raman spectrometers, a Witec 300 alpha R setup with a spectral resolution of ∼1.0 cm^{-1} and Renishaw inVia Reflex spectrometer with a spectral resolution of ∼1.6 cm^{-1}. The 532 nm laser was used as a source of illumination. A Zeiss LD EC Epiplan-Neofluar 50×/0.55 objective (Witec) and Leica N PLAN EPI 50×/0.75 objective (Renishaw) were utilized at measurements. The lateral resolution of these objectives is ∼0.6 (Witec) and ∼ 0.45 μm (Renishaw), respectively. The laser power chosen at the back of the objective was ≤∼5 mW. The edge filters with a cutoff of 90 (Witec) and 100 cm^{-1} (Renishaw) were utilized to separate the Raman signal from the excitation line. We used a Newton Andor EMCCD camera with 1600×200 pixels as a detector (for Witec set-up) and a Renishaw Centrus CCD detector with 1024×256 pixels (for Renishaw set-up).

Raman scattering mapping was performed on the *PS:LNO* sample surface with an area of 50×50 μm^2 by using the 100×100 pixel scan. Two typical patterns of Raman scattering map are depicted in Figure 4,(a). As seen in this figure, there are three distinct uniform regions on the sample surface marked with different colors (online), blue, red and green, ranging in size from a few microns to several tens of microns. These regions reveal three different Raman scattering spectra presented in Figure 4,(b). It turns out that the Raman spectrum of "green region" of *PS*:*LNO* appears to be very similar to the Raman spectrum of *LNO* single crystal powder measured by us (see Figure 5,(a)), whereas the Raman spectrum of *PS*:*LNO* "blue region" resembles the corresponding spectrum of room temperature α structural phase of SiO_2 single crystal (see Figure 5,(b)). Below we shall analyze in detail the Raman spectrum of *LNO*.

The correlation between the Raman spectrum of "blue region" of nanocomposite and those of $\alpha - SiO_2$ crystal deserves some attention. At room temperature, SiO_2 crystal adopts the α phase with $P3_121$ (No. 152) space group. According to the symmetry analysis[56], the room temperature first-order Raman spectrum of $\alpha - SiO_2$

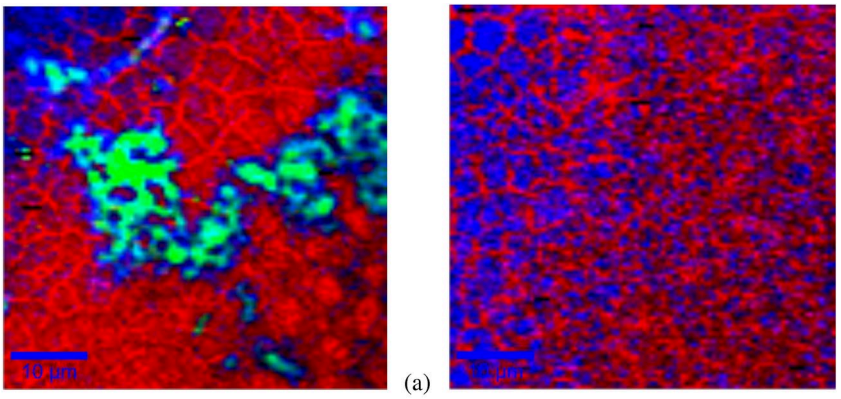

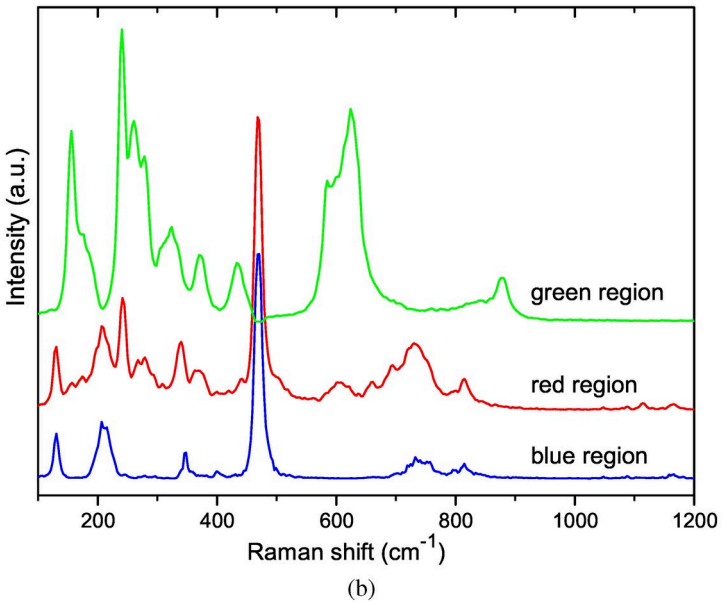

Fig. 4. (a) Raman scattering mapping of two typical areas of *PS*:*LNO* nanocomposite. The regions of the same colors (online), green, red and blue, reveal the same Raman spectra depicted in the section (b) of this figure by green, red and blue colors, respectively.

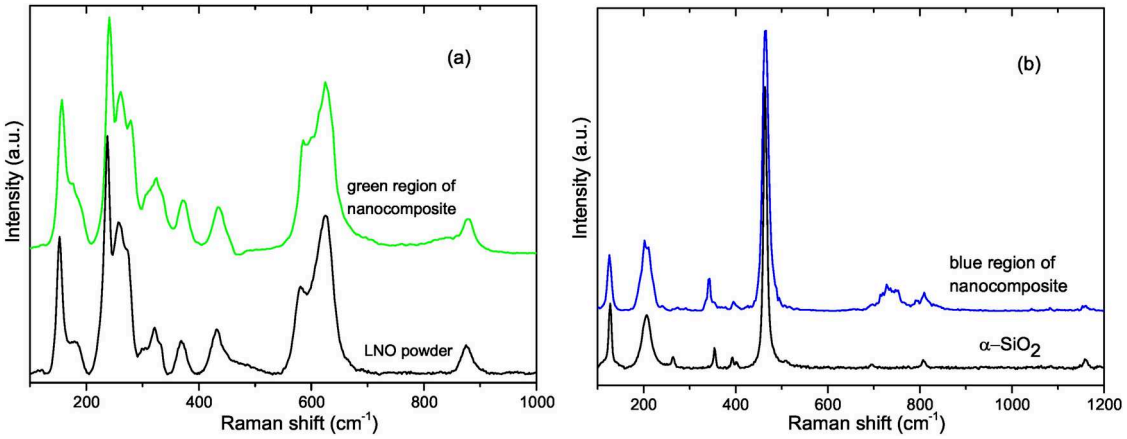

Fig. 5. (a) Comparison between Raman spectrum taken from the "green region" (online) of *PS:LNO* nanocomposite (see Figure 4) and Raman spectrum of *LNO* single crystal powder. (b) Comparison between Raman spectrum taken from the "blue region" of *PS:LNO* nanocomposite (see Figure 4) and Raman spectrum of $\alpha - SiO_2$ single crystal.

should contain not more than 12 Raman active modes ($4A_1$+8E), eight of which are two-fold degenerate owing to the two-dimensionality of E irreducible representation.

As seen in Figure 5,(b), the spectra taken from "blue region" of *PS:LNO* nanocomposite and $\alpha - SiO_2$ single crystal reveal seven same frequencies of phonon modes, *i.e.* at 126, 205, 394, 464, 696, 806 and 1160 cm^{-1}. There is some frequency disagreement between the 341 cm^{-1} mode of "blue region" of *PS:LNO* and their counterpart at 353 cm^{-1} of $\alpha - SiO_2$ spectrum. However, the main difference between both spectra depicted in Figure 5,(b) is a broad band centered near 735 cm^{-1} detected in the "blue spectrum" of *PS:LNO* nanocomposite which is absent in the spectrum of $\alpha - SiO_2$ single crystal. Despite these two peculiar spectral features observed in the "blue spectrum" of *PS:LNO* and absent in $\alpha - SiO_2$ Raman spectrum, one may conclude that the "blue spectrum" of *PS:LNO* nanocomposite (Figure 5,(b)) mainly corresponds to the spectrum of $\alpha - SiO_2$ single crystal. Note that our XRD data described in the previous section also revealed the presence of $\alpha - SiO_2$ single crystal phase in *PS:LNO* nanocomposite (see Figure 2).

Nevertheless, the main intrigue of the proper interpretation of the *PS:LNO* Raman spectrum is the elucidation of the "red part" of its spectrum (see (Figure 4,(b))). A careful inspection of the "red spectrum" reveals that, to a great extent, it combines the main features of both Raman spectra taken from $\alpha - SiO_2$ ("blue region") and *LNO* ("green region") crystals. The 127, 207, 340, 467, 810 and 1165 cm^{-1} modes are inherent to the "blue" $\alpha - SiO_2$ Raman spectrum, whereas the lines near 156, 175, 243, 277, 373, 441 and 605 cm^{-1} are consistent with the corresponding vibrational modes of the "green" *LNO* Raman spectrum (see Figure 4,(b)). This combination of spectroscopic features of different compounds, $\alpha - SiO_2$ and *LNO*, in Raman spectrum is not surprising since the optical lateral resolution of ~0.6 μm in Raman mapping is more than one order of magnitude larger than the average pore diameter, ~12.0±1.0 nm. Therefore, Raman scattering spectrum involves the information from both crystalline compounds, $\alpha - SiO_2$ and *LNO*. However, the "red spectrum" also contains the vibrational modes which have no direct counterparts either in *LNO* or in $\alpha - SiO_2$ Raman spectra. This concerns the broad band centered near 735 cm^{-1} as well as the two other lines near 660 and 694 cm^{-1}. Probably, these lines may be considered as a spectral response of the *ballen* silica microstructures and/or some new crystal phases that may arise during the structural phase transformation and recrystallization of amorphous silica during *LNO* crystal synthesis at 950 ^oC[57,58].

The performed Raman mapping gave us the information about the phase distribution on the *PS:LNO* sample surface. To shed some light on the phase morphology inside the composite sample, it is quite instructive to perform a similar Raman mapping of the freshly broken edge of *PS:LNO* membrane. The 50×50 μm^2 area (100× 100 pixel scan) of the membrane broken edge, Figure 6,(a), was chosen for Raman mapping (Figure 6,(b)). The main characteristic feature of this picture is the sequence of straight strips several μm thick, directed along the membrane pores. Different colors, red and blue, correspond to the different Raman spectra, depicted in Figure 6,(c).

The "red strips" prevail in Figure 6,(b). The magenta regions are present when the weighting factor of two components, "red" and "blue", are similar. A few "green areas" in Figure 6,(b) correspond to pure *LNO* micro-crystal regions. As seen in Figure 6,(c), the Raman spectra from the "red" and "blue strips" are rather similar, but not the same. They are also similar to the "red region" of spectra recorded from the surface of our sample (see Figure 4,(c)) which corresponds to the mixed $\alpha - SiO_2$+*LNO* phase. The main difference between the "red" and "blue" spectra in Figure 6,(c) is the various intensities of the similar lines in spectra. It is quite instructive to inspect the relation between the strongest line at 466 cm^{-1} which originates from the $\alpha - SiO_2$ phase and two strong lines at 240 and 604 cm^{-1} inherent to the *LNO* spectrum. Relations $\frac{I(466)}{I(240)}$ and $\frac{I(466)}{I(604)}$ are 1.2 and 5.7 for the "red spectrum" and 1.9 and 3.4 for the "blue spectrum" in Figure 6,(c), respectively.

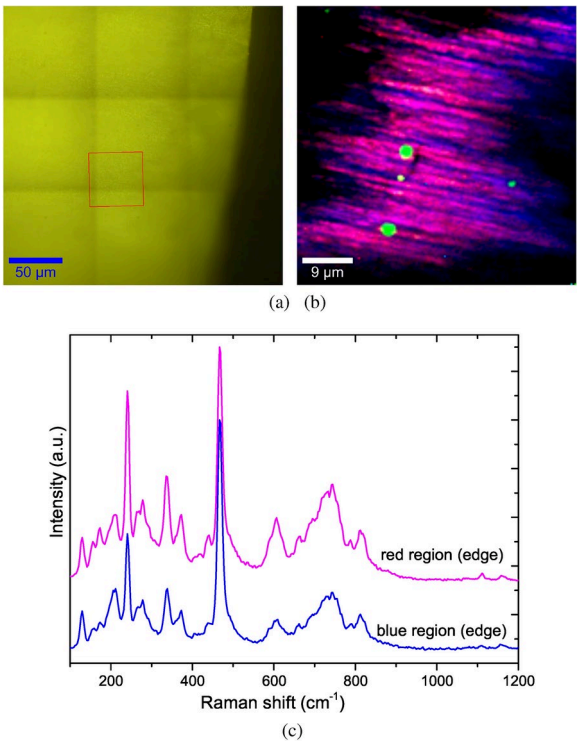

Fig. 6. (a) Optical microscope image (x50) of the freshly brocken edge of *PS:LNO* membrane. Red square indicates the area subjected to Raman scattering mapping presented in section (b). After stitching, square lines appear in the bright field image due to uneven illumination distribution, without effect on the Raman mapping. The regions of the same colors (online), red and blue, correspond to the same Raman spectra depicted in the section (c) of this figure by red and blue colors, respectively. The green dots in section (b) correspond to *LNO* regions with "green" Raman spectra depicted in Figure 4,(c)

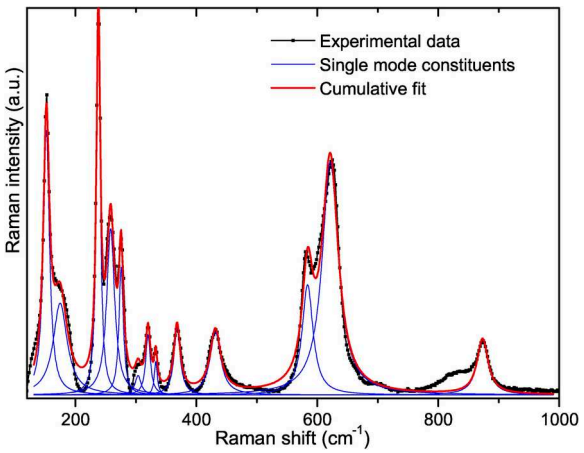

Fig. 7. Raman spectrum of the "green region" of *PS:LNO* nanocomposite approximated by the sum of 13 Lorentzian constituents.

Summarizing the results of Raman mapping both from the surface and from the broken edge, it can be stated that the *PS:LNO* nanocomposite is mainly formed from the two crystalline $\alpha - SiO_2$ and *LNO* phases. On the *PS:LNO* membrane surface, we observed the Raman response of the pure *LNO* and $\alpha - SiO_2$ regions with sizes up to several tens of microns (Figure 4,(b)). Since we detected only a few ~ 2 μm regions of pure *LNO* inside the host *PS* matrix (Figure 6,(b)), one can propose that such large areas of homogeneous *LNO* and $\alpha - SiO_2$ appeared on the surface due to the residues of the salt mixture crystallized during the high-temperature synthesis of *LNO* at 950 °C. Moreover, the growth of pure *LNO* and $\alpha - SiO_2$ regions depends on the synthesis conditions, which are different on the surface and inside the host porous matrix, where the spatial confinement is relevant.

Let us inspect more carefully the Raman spectrum of the "green region" of *PS:LNO* nanocomposite (see Figure 4,(b)). At room temperature, LNO crystal adopts a rhombohedral symmetry with *R3c* (#161) space group (Z=6)[52]. Since the primitive cell contains two structural units, the 30 normal modes are classified in the Brillouin zone centre according to irreducible representations of the *R3c* group as follows,

Γ=5A_1(R,IR)+5A_2(inact.)+10E(R,IR),

where R and IR imply Raman and infrared activity, respectively. Normal modes of $A2$ symmetry are neither Raman nor IR active. The E irreducible representation is two-dimensional, which implies that the modes of E symmetry are twice degenerate. Since three modes A_1+E are acoustic modes, one may expect 13 different optic phonon modes in the Raman spectrum, i.e., 4 A_1+ 9 E. The experimental *LNO* Raman spectrum ("green" spectrum in Figure 4,(b)) may be fitted by the sum of 13 Lorentzian constituents. However, the 13 Raman modes observed by us do not necessarily correspond to 13 modes, symmetry allowed for *LNO* crystal, as it follows from the group-theoretical analysis of lattice dynamics. To perform a more rigorous assignment of Raman modes observed in *PS:LNO*, we compare our experimental data with those presented in Ref. [54], whose symmetry assignment was done based on *ab initio* calculations (see Table 1). As follows from this table, some modes detected in our *PS:LNO* spectrum correspond to

longitudinal modes, i.e., 175 (LO_1, E symmetry), 304 (LO_3, E) and 874 cm^{-1} (LO_9, E). The transverse TO_1 and longitudinal LO_1 parts of the same optical mode O_1 of E type are visible in our spectrum since we recorded the *LNO* spectrum from the powder material.

The appearance of E symmetry LO_9 mode near 874 cm^{-1} in Raman spectrum deserves a special attention. First of all, the transverse counterpart of this O_9 mode is placed near 661 cm^{-1} (Ref.[54]), signifying more than 200 cm^{-1} TO-LO splitting. This huge splitting implies an existence of a strong macroscopic electric field in the dielectric *LNO* crystal. Secondly, closer inspection of the lattice dynamical nature of LO_9 (E) mode based on the *eigen*vector information about this mode may shed some light on the broad low-frequency shoulder neighboring to this LO_9 (E) mode of *PS:LNO* Raman spectrum (see Figure 7). According to the paper[54], the TO_9 (E) mode is a pure internal mode of the oxygen subsystem. Moreover, this TO_9 (E) mode is very sensitive to the short-range crystal environment, which significantly changes its Raman intensity in $LiTaO_3$ comparing to *LNO*. One may suppose that the observation of the broad shoulder within the 820-860 cm^{-1} in *PS:LNO* spectrum may be the consequence of spatial nanoconfinement effect which can distort the crystal field of *LNO* nanocrystals confined inside the silica nanochannels.

Second harmonic generation (SHG)

Because of a large diffusive light scattering by *PS:LNO* nanocomposite samples, the NLO optical properties have been studied by exploring the SHG response using both transmittance and reflectance geometries. The experimental setups are sketched in Figures 8(a) and 9(a), respectively. The SHG setup in the transmission geometry is similar to that used in our recent studies[7,8]. A picosecond Nd:YAG laser (λ = 1064 nm, E_p = 100 μJ, τ = 30 ps), repetition rate 10 Hz has been used as a fundamental pumping source. The samples were placed on a rotating optical stage to make measurements at different (azimuthal) incident angles α, whereas a rotating half-wave plate ($\lambda/2$) was used to set the polarization direction of the pumping light, with the aim of examining the anisotropy of SHG conversion efficiency in *PS:LNO* nanocomposite samples. In both SHG setups, a long-focus lens L_1 is used to adjust an appropriate (non-destructive) power density of the light incident on the nanocomposite sample, while a high-aperture short-focus lens L_2 ensures efficient collection (solid angle of 1. 5 sr) of the diffusely transmitted or diffusely reflected SHG light, which is then filtered by an interference filter F (λ = 532 nm) and detected by a photomultiplier (PM) with a boxcar averager (integration time 0.1 s). Azimuthal scans were performed in one-degree steps by averaging over 20 light pulses for each angular position of the sample.

Our data	Paper[54]	Mode assignment[54]
152	151	TO_1, E
175	192	LO_1, E
238	237	TO_2, E
258	252	TO_1, A_1
276	275	TO_2, A_1
304	297	LO_3, E
320	320	TO_4, E
333	333	TO_3, A_1
368	367	TO_5, TO_6, E
432	432	TO_7, E
584	580	TO_8, E
622	633	TO_4, A_1
874	877	LO_9, E

Table 1. Comparison between the phonon frequencies (in cm^{-1}) obtained from the fit of *PS:LNO* Raman spectrum (Figure 7) and the experimental Raman frequencies of LNO single crystal detected in Ref. [54].

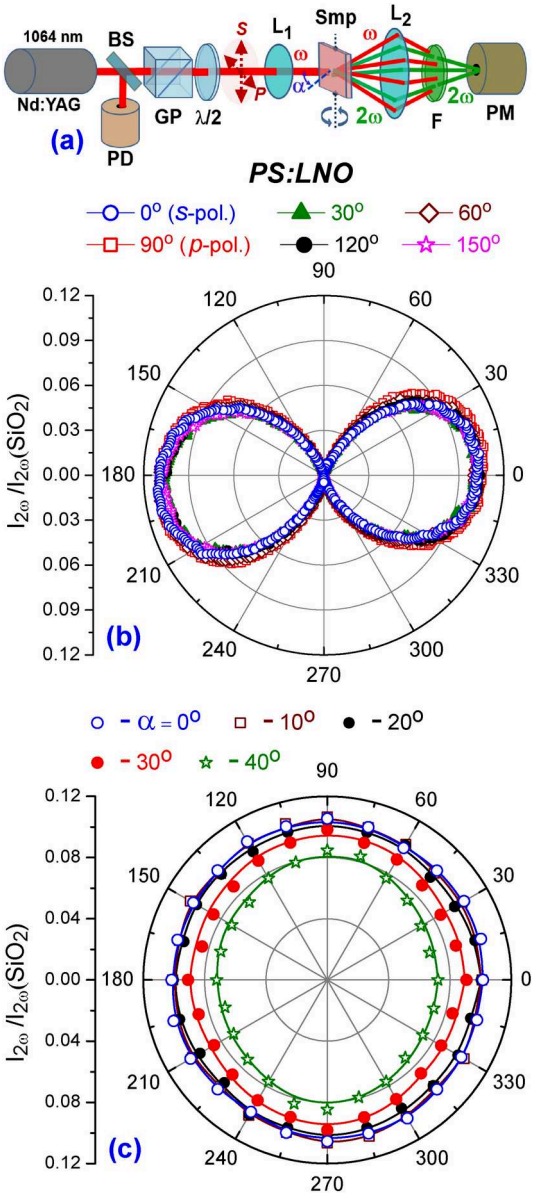

Fig. 8. Second harmonic generation (SHG) from *PS:LNO* nanocomposite membranes in the straight diffuse transmission geometry. Sec.(a): Sketch of the SHG setup: **Nd:YAG**, laser (λ= 1064 nm, E_p = 100 μJ, τ= 30 ps); **λ/2**, half-wave plate; **GP**, Glan polarizer; $\mathbf{L}_1$ and $\mathbf{L}_2$, lenses; **Smp**, measured sample; **F**, interference filter (532 nm); **PD**, photodiode; **BS**, beam splitter; **PM**, photomultiplier. The rotating half-wave plate serves to set a light polarization direction. Sec.(b): Azimuthal dependences (polar plots) of the SHG response measured from the *PS:LNO* membrane for different directions of pumping light polarization: 0° (*s*-polarization), 30°, 60°, 90° (*p*-polarization), 120° and 150°, see labels. Sec.(c): Light polarization dependences of SHG response from the *PS:LNO* membrane for five fixed incident angles α [0°, 10°, 20°, 30° and 40°], see labels.

To qualitatively characterize the SHG conversion efficiency, the measured SHG response of the *PS:LNO* composite membrane is compared to the SHG response of the reference sample, which in the case of the transmission geometry is a 1 mm thick crystal quartz (α-SiO_2) plate set in *ooo* coupling geometry ($\chi^{(2)}_{111}$ component). The setup presented in Figure 8,(a) actually corresponds to the Maker fringe scheme used in previous studies, see e.g.[7,8]. However, the azimuthal dependences of the SHG response (see polar plots in Figure 8(b)) do not show fringes, but reveal a broad angular pattern typical of diffusely scattered SHG emission, apparently caused by light dephasing and decoherence due to diffuse multiple scattering. Moreover, the angular dependences of the SHG response measured for different directions of pumping light polarization [0° (*s*-polarization), 30°, 60° , 90° (*p*-polarization), 120° and 150°] overlap within experimental accuracy and appear to be consistent with a practically circular shape of the light polarization dependences of the SHG response (Figure 8,(c)) recorded for different incident angles (α=0°, 10°, 20° and 30°) of the pumping light beam. The slight ellipticity, extended along the *p*-polarization direction, noticeable at larger incident angles (e.g. α=40°), should be attributed to a

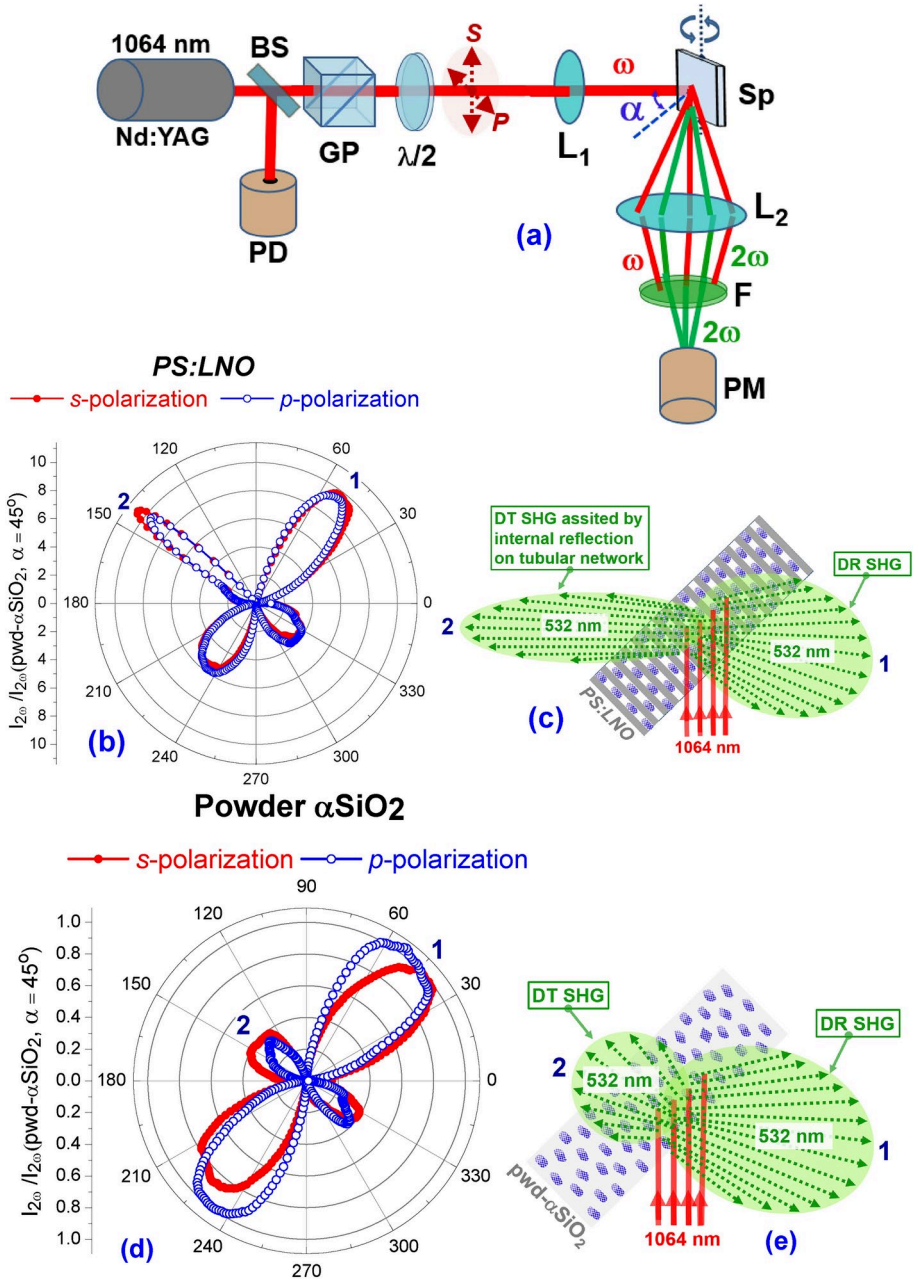

Fig. 9. Second harmonic generation (SHG) from *PS:LNO* nanocomposite membranes in the 90° diffuse reflectance/transmittance geometry. Sec.(a): Sketch of the SHG setup: Components (**Nd:YAG**, **λ/2**, **GP**, $\mathbf{L_1}$, $\mathbf{L_2}$, **Sp**, **F**, **PD**, **PM**) are described in Fig. 8,(a). Sec.(b) and Sec.(d) present azimuthal dependences (polar plots) of SHG response measured in the 90°-geometry from *PS:LNO* membrane and compressed microcrystalline layer of α-SiO_2, respectively, for *p* and *s* directions of pumping light polarization, see labeled. Insets in Secs.(c) and (e) sketch the diffuse transmittance (DT) and diffuse reflectance (DR) SHG emissions, see also labeled as **2** and **1** in Secs.(b) and (d), respectively. Unusually large, but azimuthally narrow DT SHG emission from *PS:LNO*, sketched in Sec.(c), is apparently assisted by lateral reflection from tubular channel network of *PS*-matrix. DR SHG emission intensity from micropowder α-SiO_2-layer, measured at α=45°, is taken as the reference value for characterization of the SHG conversion efficiency.

rising difference in the reflection from the sample surface between *s* and *p* components of the polarized pumping light when approaching the Brewster angle, i.e., in accordance with the Fresnel equations. Direct experimental examination indeed proves this statement: the angular polarization diagram does not change while rotating the tilted nanocomposite sample around the axis normal to it. Taken together, the SHG effect appears to exhibit spatial isotropy with respect to both the directions of light propagation and its polarization.

This appears to be consistent with the specific textural morphology of *PS:LNO* nanocomposites, characterized by orientational disorder of the deposited *LNO* nanocrystals, as suggested by XRD studies. In the nanocomposite

PS:LNO media, the SHG light may be generated by the guest *LNO* nanocrystals as well as the partially crystallized silica matrix. Similarly to other opaque NLO composite materials, as e.g. silica-benzil nanocomposites[8], the SHG intensity is proportional to the transmission factor k_t accounting for reduction of the converted light due to its diffuse multiple scattering. Direct measurements on several nanocomposite samples gives the k_t-value of 0.01÷0.12. Accordingly, the expected performance of hypothetically transparent (i.e., uniformly filled) composite *PS:LNO* membranes in the normal transmission geometry is larger by a factor of k_t^{-1} than the measured one ($0.11 \cdot I_{2\omega}(\chi^{(2)}_{111}(\alpha\text{SiO}_2)$, see Figure 8,(b)), which gives the hypothetical ratio $I_{2\omega}(PS{:}LNO)/I_{2\omega}(\chi^{(2)}_{111}(\alpha\text{-SiO}_2))$ approximately equal to 9÷11.

A more precise characterization of the NLO conversion efficiency can be provided by relying on SHG measurements in the reflection geometry (Figure 9), using a $\sim$150μm thick layer of compressed microcrystalline α-SiO_2 powder as a reference. The photomultiplier (PM) is set in a stationary 90°-geometry with respect to the incident laser beam (Figure 9,(a)). The sample is rotated over 360° in one-degree angular step starting from its normal position (α=0°). Here, it should be emphasized that the sample positions in angular quadrants 0°-90° (180°-270°) and 90°-180° (270°-360°) are associated with two different regimes of the emitted SHG light, i.e., the regimes of diffuse reflectance (DR) and diffuse transmittance (DT), respectively, as sketched in inserts in Figures 9(c) and 9(e), respectively. Figures 9(b) and 9(d) show the polar plots of the SHG response vs the incident angle α for the nanocomposite *PS:LNO* and the reference powder α-SiO_2 samples, respectively, recorded for *p* and *s* polarizations of the incident light. The DR SHG-response (α=45°) of α-SiO_2 powder serves here as a reference value for quantitative characterization of the NLO optical conversion efficiency. The DR SHG response of the *PS:LNO* nanocomposite, characterized by ratio $I_{2\omega}(PS{:}LNO)/I_{2\omega}(\text{pwd-}\alpha\text{-SiO}_2, \alpha = 45°)$, reaches its maximum value of 9.4 at α=50°, which is consistent with the SHG performance evaluated above for hypothetically transparent composite *PS:LNO* membranes based on SHG measurements in the normal transmitting geometry. The strong drop in SHG response at approaching incident angles $\alpha = \pm 90°$ must be due to (i) an increase of reflectivity of the fundamental beam from the membrane surface and (ii) a decrease of the fundamental laser intensity in the sample due to the increase in the effective scattering path length. However, as one approaches normal incidence angles (α=0°,180°), the increasing scattering path length for the converted radiation directly causes a strong decrease in the output SHG response. Furthermore, since $I_{2\omega}(PS{:}LNO) \gg I_{2\omega}(\text{pwd-}\alpha\text{-SiO}_2)$, one can conclude that the contribution of guest *LNO* nanocrystals to the second-order macroscopic optical nonlinearity is highly dominant compared to the partially crystallized host *PS* matrix. However, one should admit that the conversion efficiency of the DR SHG response from the opposite membrane face (α=130°) is much smaller, $I_{2\omega}(PS{:}LNO)/I_{2\omega}(\text{pwd-}\alpha\text{-SiO}_2, \alpha = 45°)$=6. Apparently, this is caused by the conical shape of the nanochannels[55] and, accordingly, by the inhomogeneous morphology of the *LNO* nanocrystals embedded into tubular PS-matrix. The conicity of the pores results from the unidirectional *p*Si etching process. It turns out that the fundamental laser beam incident on the membrane side of conical channels with smaller inlet diameter causes a considerably stronger DR SHG response (marked as 1 in Figure 9,(e)) compared to the opposite side of the membrane, whereas for DT SHG (marked as 2 in Figure 9,(e)) it is vice versa. A more detailed description of such angular behaviour requires consideration of multiply scattering effects occurring in the case of nonuniform spatial distribution of nanocrystals along the conical nanochannels. The development of an appropriate theoretical model is beyond the scope of this study and may be considered elsewhere.

Nanocomposite membranes *PS:LNO* show a NLO behavior unusual for conventional diffuse scattering (opaque) media. Because of multiple scattering and hence limited penetration depth of both fundamental and SHG converted light, the intensity of DT SHG light in such media is usually considerably smaller than that of DR SHG light. A prominent example is the compressed micropowder α-SiO_2 layer, see labeled 2 and 1 in Figure 9,(e), respectively. *PS:LNO*, in contrast, reveals the intensity of DT SHG light even slightly higher than DR SHG light, wherein its directional diagram is twice as narrow compared to the DR SHG light, see labeled by 2 and 1 in Figure 9,(c) for comparison. Such an amazing behavior, probably associated with the internal array of tubular nanochannels, will need a more detailed theoretical consideration. However, this is beyond the scope of the actual study and will be considered elsewhere. Despite the fundamental interest, such back-reflected SHG emission deserves special analysis in the context of its potential applications.

Conclusions

In conclusion, we demonstrate a hybrid nanocomposite combining *PS* as mesoporous host media and guest *LNO* nanocrystals embedded into tubular nanochannels. The synthesis methodology is based on a precursor mixture solution of lithium and niobium salts with its subsequent calcination in nanochannels of mesoporous silica. In such a hybrid composition, the *PS* matrix provides a mechanically stiff scaffold, whereas the NLO optical functionality results from the specific properties of the embedded *LNO* nanocrystals. HRTEM and XRD techniques evidence trigonal *LNO* nanocrystals inside the *PS* nanochannels indicating their completely random texture morphology. Annealing at high temperatures (950°C) during calcination also leads to partial crystallization of the *PS*-matrix with the formation of trigonal α-SiO_2 nanocrystals.

The Raman spectra of *PS:LNO* nanocomposite reveal the three structural crystalline phases of different sizes. Two of them, *LNO* and α-SiO_2 phases are of μm-scale.These phases are clearly observable on the sample surface. However, the main part of *PS:LNO* volume consists of the combined phase which involves the α-SiO_2 crystalline phase of host membrane and *LNO* nanocrystals embedded into the membrane. This third phase also contains some amount of unknown phase or some new silica phases probably appearing during the high temperature recrystallization of amorphous silica during the synthesis of *LNO* nanocrystals. Despite a very close resemblance between the Raman spectra of *LNO* microsized regions of nanocomposite and that of the bulk *LNO* crystal, the Raman spectrum of *PS:LNO* composite exhibits specific features that are not characteristic of its bulk *LNO* counterpart. In particular, the broad low-frequency shoulder in the region of 820-860 cm^{-1}, adjacent to the

Raman LO_9(E) band, apparently indicates a spatial nanoconfinement effect resulting from the finite size of the *LNO* nanocrystals, which perturbs the macroscopic crystal field and, consequently, the LO-TO splitting.

In terms of overall optical characterization, the *PS*:*LNO* membranes are opaque and highly light-scattering materials, apparently due to the randomly distributed *LNO* nanocrystals acting as light scattering centers. Due to this, the SHG response has been studied using both transmittance and reflectance geometries. The SHG reveals no Maker fringes in the transmittance geometry, apparently due to the light dephasing and decoherence associated with diffuse multiple scattering. Its azimuthal dependence exhibits a broad angular diagram of diffuse scattered SHG emission, which is independent of the polarization direction of the incident light indicating a spatial isotropy of SHG effect. It appears to be consistent with specific textural morphology of *PS*:*LNO* nanocomposites, i.e., orientationally disordered *LNO* nanocrystals deposited into silica nanochannels, as suggested by XRD studies.

LNO nanocrystals, randomly oriented and locally separated in *PS* nanochannels, cause a considerable multiple scattering of light, as well as its depolarization resulting thus in considerable reduction of macroscopic (bulk) conversion efficiency. Accordingly, mesoporous tubular host media uniformly filled with guest functional crystalline material remains a technological challenge and will require further efforts to find suitable solutions to improve their performance.

In *PS*:*LNO* nanocomposite, the SHG light may be generated by guest LNO nanocrystals as well as by partially crystallized silica matrix. To ascertain relevant contributions to the SHG effect, nanocomposite *PS*:*LNO* samples were measured in the 90°-reflection geometry and compared with micropowder α-SiO_2 sample as the reference. The contribution of guest *LNO* nanocrystals to the second-order macroscopic optical nonlinearity was found to be strongly dominant compared to the partially crystallized host *PS*-matrix. Moreover, *PS*:*LNO* membranes reveal the NLO behavior unusual for conventional diffuse scattering (opaque) media. The diffuse transmittance (DT) intensity of SHG light is extremely high, even slightly exceeding the intensity of diffused reflectance (DR) SHG light emitted in the opposite direction, whereas its directional diagram is twice as narrow compared to the DR SHG light. Such anomalous behavior, probably related to the internal reflection from the tubular nanochannel network, will require more detailed theoretical considerations aimed at shedding light on the specific physical mechanisms responsible for this effect. Despite the fundamental interest, the anomalous back-reflected SHG emission revealed in *PS*:*LNO* nanocomposite membranes expands new prospects for their photonic and NLO applications. Understanding and controlling the textural morphology in all-inorganic nanocrystalline composites as well as its relationships with material properties can lead to the development of novel efficient NLO materials for light energy conversion.

Received: 6 May 2024; Accepted: 7 October 2024
Published online: 16 October 2024

References

1. Nguyen, T.-P., Polymer-based nanocomposites for organic optoelectronic devices. A review, Surf. Coat. Tech. 206 (2011) 742-752, https://doi.org/10.1016/j.surfcoat.2011.07.010
2. Abdel-Salam, A. I., Awad, M. M., Soliman, T. S. & Khalid, A. The effect of graphene on structure and optical properties of CdSe nanoparticles for optoelectronic application. *J. Alloy. Compd.* **898**, 162946. https://doi.org/10.1016/j.jallcom.2021.162946 (2022).
3. Yassin, A. Y. Synthesized polymeric nanocomposites with enhanced optical and electrical properties based on gold nanoparticles for optoelectronic applications. *J. Mater. Sci: Mater. Electron.* **34**, 46. https://doi.org/10.1007/s10854-022-09402-3 (2023).
4. Sagadevan, S. et al. Functionalized graphene-based nanocomposites for smart optoelectronic applications. *Nanotech. Rev.* **10**, 605–635. https://doi.org/10.1515/ntrev-2021-0043 (2021).
5. Jin, Z. et al. Graphdiyne:ZnO nanocomposites for high-performance UV photodetectors. *Adv. Mater.* **28**, 3697–3702. https://doi.org/10.1002/adma.201600354 (2016).
6. Kityk, A. V. et al. Dynamic Kerr and Pockels electro-optics of liquid crystals in nanopores for active photonic metamaterials. *Nanoscale* **13**, 18714–18725. https://doi.org/10.1039/D1NR04282C (2021).
7. Waszkowska, K. et al. Anisotropic confinement of chromophores induces second-order nonlinear optics in a nanoporous photonic metamaterial. *Opt. Lett.* **46**, 845–848. https://doi.org/10.1364/OL.416948 (2021).
8. Karout, H. . El. et al. Second harmonic generation on crystalline organic nanoclusters under extreme nanoconfinement in functionalized silica-benzil composites. *Sci. Rep.* **13**, 9943. https://doi.org/10.1038/s41598-023-37147-4 (2023).
9. Khalid, A., Ahmed, R. M., Taha, M. & Soliman, T. S. Fe_3O_4 nanoparticles and Fe_3O_4@SiO_2 core-shell: synthesize, structural, morphological, linear, and nonlinear optical properties. *J. Alloy. Compd* **947**, 169639. https://doi.org/10.1016/j.jallcom.2023.169639 (2023).
10. Sentker, K. et al. Quantized Self-Assembly of Discotic Rings in Nanopores. *Phys. Rev. Lett.* **120**, 06780111. https://doi.org/10.1103/PhysRevLett.120.067801 (2018).
11. Sentker, K. et al. Self-assembly of liquid crystals in nanoporous solids for adaptive photonic metamaterials. *Nanoscale* **11**, 23304–23317. https://doi.org/10.1039/C9NR07143A (2019).
12. Shchur, Y. & Kityk, A. V. Ordered $PbHPO_4$ nanowires: Crystal structure, energy bands and optical properties from first principles, computation. *Mater. Sci.* **138**, 1–9. https://doi.org/10.1016/j.commatsci.2017.06.008 (2017).
13. Shchur, Y., Pavlyuk, O., Andrushchak, A. S., Vitusevich, S. & Kityk, A. V. Porous Si partially filled with water molecules - crystal structure, energy bands and optical properties from first principles. *Nanomaterials* **10**(396), 1–17. https://doi.org/10.3390/nano10020396 (2020).
14. Lehmann, V., Stengl, R. & Luigart, A. On the morphology and the electrochemical formation mechanism of mesoporous silicon. *Mat. Sci. Eng. B* **69–70**, 11–22. https://doi.org/10.1016/S0921-5107(99)00286-X (2000).
15. Salonen, J., Lehto, V.-P. & Laine, E. Thermal oxidation of free-standing porous silicon films. *Appl. Phys. Lett.* **70**, 637–639. https://doi.org/10.1063/1.118294 (1997).
16. Całus, S., Rau, D., Huber, P. & Kityk, A. V. Influence of nanoconfinement on the nematic behavior of liquid crystals. *Phys. Rev. E* **86**, 021701. https://doi.org/10.1103/PhysRevE.86.021701 (2012).
17. Całus, S. et al. Paranematic-to-nematic ordering of a binary mixture of rodlike liquid crystals confined in cylindrical nanochannels. *Phys. Rev. E* **89**, 062501. https://doi.org/10.1103/PhysRevE.89.062501 (2014).
18. Shchur, Y. et al. Paraelectric KH_2PO_4 nanocrystals in monolithic mesoporous silica: Structure and lattice dynamics. *J. Alloy. Compd.* **868**, 159177. https://doi.org/10.1016/j.jallcom.2021.159177 (2021).

19. Shchur, Y. et al. On the issue of textured crystallization of $Ba(NO_3)_2$ in mesoporous SiO_2: Raman spectroscopy and lattice dynamics analysis. *Spectrochim. Acta A* **275**, 121157. https://doi.org/10.1016/j.saa.2022.121157 (2022).
20. Shchur, Y. et al. Nanoarhitectonics of inorganic-organic silica-benzil composites: Synthesis, nanocrystal morphology and micro-Raman analysis. *Nanomater.* **13**, 1913. https://doi.org/10.3390/nano13131913 (2023).
21. Warner, A. W., Onoe, M. & Coquin, G. A. Determination of Elastic and Piezoelectric Constants for Crystals in Class (3m). *J. Acoust. Soc. Am.* **42**, 1223–1231. https://doi.org/10.1121/1.1910709 (1967).
22. Weis, R. S. & Gaylord, T. K. Lithium niobate: Summary of physical properties and crystal structure. *Appl. Phys. A* **37**, 191–203. https://doi.org/10.1007/BF00614817 (1985).
23. Cho, Y. & Yamanouchi, K. Nonlinear, elastic, piezoelectric, electrostrictive, and dielectric constants of lithium niobate. *J. Appl. Phys.* **61**, 875–887. https://doi.org/10.1063/1.338138 (1987).
24. Tarumi, R., Matsuhisa, T., Shibutani, Y., Low temperature elastic constants and piezoelectric coefficients of $LiNbO_3$ and $LiTaO_3$: resonant ultrasound spectroscopy measurement and lattice dynamics analysis, Jpn J Appl Phys, 51 (2012) 07GA02, https://doi.org/10.1143/JJAP.51.07GA02
25. Schlarb, U. & Betzler, K. Refractive Indices of Lithium Niobate as a Function of Temperature, Wavelength, and Composition: A Generalized Fit. *Phys. Rev. B* **48**, 15613–15620. https://doi.org/10.1103/PhysRevB.48.15613 (1993).
26. Moretti, L., Iodice, M., Della Corte, F. & Rendina, I. Temperature dependencies of the thermo-optic coefficient of lithium niobate, from 300 to 515 K in the visible and infrared regions. *J. Appl. Phys.* **98**, 036101. https://doi.org/10.1063/1.1988987 (2005).
27. Sando, D. M., & Jaatinen, E., A method to remotely measure temperature change in a lithium niobate crystal using birefringence, J. Eur. Opt. Soc.-Rapid, 4, 09011, (2009) https://doi.org/10.2971/jeos.2009.09011
28. Ashkin, A. et al. Optically-induced refractive index inhomogeneities in $LiNbO_3$ and $LiTaO_3$. *Appl. Phys. Lett.* **9**, 72–74. https://doi.org/10.1063/1.1754607 (1966).
29. Buse, K., Imbrock, J., Krätzig, E., & Peithmann, K., Photorefractive Effects in $LiNbO_3$ and $LiTaO_3$. In: P. Günter, J. P. Huignard (eds) Photorefractive Materials and Their Applications 2. Springer Series in Optical Sciences, Springer, New York, vol. 114 83-126, (2007) https://doi.org/10.1007/0-387-34081-5_4
30. Andrushchak, A. S., Mytsyk, B. G., Demyanyshyn, N. M., Kaidan, M. V., Yurkevych, O. V., Solskii, I. M., Kityk, A. V., & Schranz, W., Spatial anisotropy of linear electro-optic effect in crystal materials: I. Experimental determination of electro-optic tensor in $LiNbO_3$ by means of interferometric technique, Opt. Lasers Eng. 47, 31-38, (2009) https://doi.org/10.1016/j.optlaseng.2008.08.005.
31. Andrushchak, A. S., Mytsyk, B. G., Demyanyshyn, N. M., Kaidan, M. V., Yurkevych, Dumych, S. S., Kityk, A. V., & Schranz, W., Spatial anisotropy of linear electro-optic effect in crystal materials: II. Indicative surfaces as efficient tool for electro-optic coupling optimization in $LiNbO_3$, Opt. Lasers Eng. 47, 24-30, (2009) https://doi.org/10.1016/j.optlaseng.2008.08.007
32. Wong, K. K. (ed), Properties of Lithium Niobate, INSPEC:IET, London (2002).
33. Andrushchak, A. S. et al. Complete sets of elastic constants and photoelastic coefficients of pure and MgO-doped lithium niobate crystals at room temperature. *J. Appl. Phys.* **106**, 073510. https://doi.org/10.1063/1.3238507 (2009).
34. Cantelar, E. et al. Multi-line NIR-RGB emission in Nd:$LiNbO_3$ RPE optical waveguides. *Electron. Lett.* **43**, 632–633. https://doi.org/10.1049/el:20070334 (2007).
35. Djukic, D. et al. Electro-optically tunable second-harmonic-generation gratings in ion-exfoliated thin films of periodically poled lithium niobate. *Appl. Phys. Lett.* **90**, 171116. https://doi.org/10.1063/1.2728739 (2007).
36. Wang, C. et al. Second harmonic generation in nano-structured thin-film lithium niobate waveguides. *Opt. Express* **25**, 6963–6973. https://doi.org/10.1364/OE.25.006963 (2017).
37. Chang, L. et al. Thin film wavelength converters for photonic integrated circuits. *Optica* **3**, 531–535. https://doi.org/10.1364/OPTICA.3.000531 (2016).
38. Wang, C. et al. Metasurface-assisted phase-matching-free second harmonic generation in lithium niobate waveguides. *Nat. Commun.* **8**, 2098. https://doi.org/10.1038/s41467-017-02189-6 (2017).
39. Kim, T.-H. et al. Effect of Lithium Compensation on UV-VIS and IR Absorption Spectra in $LiNbO_3$ Crystals. *J. Kor. Phys. Soc.* **41**, 390–394 (2002).
40. Polgar, K., Peter, A., Kovacs, L., Corradi, G. & Szaller, Z. Growth of stoichiometric $LiNbO_3$ single crystals by top seeded solution growth method. *Journal of Crystal Growth* **177**, 211–216. https://doi.org/10.1016/s0022-0248(96)01098-6 (1997).
41. Hilberg, R. P. & Hook, W. R. Transient Elastooptic Effects and Q-Switching Performance in Lithium Niobate and KDP Pockels Cells. *Appl. Opt.* **9**, 1939–1940. https://doi.org/10.1364/AO.9.001939 (1970).
42. Jelinkova, H. et al. $LiNbO_3$ Pockels cell for Q-switch of Er:YAG laser. *Laser Phys. Lett.* **1**, 59–64. https://doi.org/10.1002/lapl.200310020 (2004).
43. Lee, T. H., Hwang, F. T., Shay, W. T. & Lee, C. T. Electromagnetic field sensor using Mach-Zehnder waveguide modulator. *Microw. Opt. Techn. Lett.* **48**, 1897–1899. https://doi.org/10.1002/mop.21776 (2006).
44. Lee, T. H., Wu, P. I. & Lee, C. T. Intergraded $LiNbO_3$ electrooptical electromagnetic field sensor. *Microw. Opt. Techn. Lett.* **49**, 2312–2314. https://doi.org/10.1002/mop.22715 (2007).
45. Li, M. et al. Lithium niobate photonic-crystal electro-optic modulator. *Nat. Commun.* **11**, 4123. https://doi.org/10.1038/s41467-020-17950-7 (2020).
46. Mok, F. Angle-multiplexed storage of 5000 holograms in lithium niobate. *Opt. Lett.* **18**, 915–917. https://doi.org/10.1364/OL.18.000915 (1993).
47. Li, G., Chen, Y., Jiang, H. & Chen, X. Broadband sum-frequency generation using d_{33} in periodically poled $LiNbO_3$ thin film in the telecommunications band. *Opt. Lett.* **42**, 939–942. https://doi.org/10.1364/OL.42.000939 (2017).
48. Chen, J. Y. et al. Efficient parametric frequency conversion in lithium niobate nanophotonic chips. *OSA Continuum* **2**, 2914–2924. https://doi.org/10.1364/OSAC.2.002914 (2019).
49. Singh, K., Saodekar, P. V. & Bhoga, S. S. Effect of stoichiometry on the thermal expansion coefficients of lithium niobate single crystals. *Bull. Mater. Sci.* **21**, 469–474. https://doi.org/10.1007/BF02790348 (1998).
50. Grigas, A. & Kaskel, S. Synthesis of LiNbO3 nanoparticles in a mesoporous matrix. *Beilstein J. Nanotech.* **2**, 28–33. https://doi.org/10.3762/bjnano.2.3 (2011).
51. Całus, S., Kityk, A. V. & Huber, P. Molecular ordering of the discotic liquid crystal HAT6 confined in mesoporous solids. *Micropor. Mesopor. Mat.* **197**, 26–32. https://doi.org/10.1016/j.micromeso.2014.05.036 (2014).
52. Abrahams, S. C. & Marsh, P. Defect structure dependence on composition in lithium niobate. *Acta Cryst. B* **42**, 61–68. https://doi.org/10.1107/S0108768186098567 (1986).
53. Patterson, A. L. The Scherrer formula for X-ray particle size determination. *Phys. Rev.* **56**, 978–982. https://doi.org/10.1103/PhysRev.56.978 (1939).
54. Sanna, S. et al. Raman scattering efficiency in $LiTaO_3$ and $LiNbO_3$ crystals. *Phys. Rev. B* **91**, 224302. https://doi.org/10.1103/PhysRevB.91.224302 (2015).
55. Thelen, M., Bochud, N., Brinker, M., Prada, C. & Huber, P. Laser-excited elastic guided waves reveal the complex mechanics of nanoporous silicon. *Nat. Com.* **12**, 3597. https://doi.org/10.1038/s41467-021-23398-0 (2021).
56. Ichikawa, S., Suda, J., Sato, T. & Suzuki, Y. Lattice dynamics and temperature dependence of the first-order Raman spectra for α -SiO_2 crystals. *J. Raman Spectrosc.* **34**, 135. https://doi.org/10.1002/jrs.966 (2003).
57. Trepmann, C. et al. Quartz and cristobalite ballen in impact melt rocks from the Ries impact structure, Germany, formed by dehydration of shock-generated amorphous phases. *Meteorit. Planet. Sci.* **55**, 2360. https://doi.org/10.1111/maps.13590 (2020).
58. Kingma, K. J. & Hemley, R. J. Raman spectroscopics study of microcrystalline silica. *American Mineralogist* **79**, 269 (1994).

Acknowledgements
Authors are grateful for the assistance and support of the Ernst Ruska-Centre for Microscopy and Spectroscopy with Electrons (ER-C-1) at Forschungszentrum Jülich in TEM measurements. Calculations have been carried out using resources provided by the Wroclaw Centre for Networking and Supercomputing (http://wcss.pl), grant No. 160.

Author contributions
Y.S.: conceptualization, methodology, symmetry analysis, Raman spectra analysis; Y.S. and A.V.K. wrote the main manuscript text; H.E.K.: methodology of non-linear optical experiment, SHG; B.S.: analysis of the non-linear optical data, project management; G.B.: sample preparation, Raman scattering mapping, data analysis; D.P.: sample preparation, SEM, HRTEM, data analysis; S.V.: SEM, HRTEM, data analysis, project management; A.A.: data analysis, general project management; P.H.: sample preparation, XRD methodology, data analysis; A.V.K.: conceptualization, methodology, sample preparation, analysis of the non-linear optical data, XRD.

Funding
A.A. acknowledges the project "Nanoarhitectonics" (number 0124U000826) supported by Ministry of Education and Science of Ukraine. The presented results are part of a project that has received funding from the European Union's Horizon Europe research and innovation programme under the Marie Sk?odowska-Curie Grant agreement no. 101086493. A.V.K. acknowledges the project cofinanced by the Polish Ministry of Education and Science under the program "Co-financed international projects", project no. W26/HE/2023 (Dec. MEiN 5451/HE/2023/2). Y.S. acknowledges the financial support from the National Research Foundation of Ukraine (grant no. 2023.05/0019). P.H. was supported by the Deutsche Forschungsgemeinschaft (DFG, German Research Foundation, CRC 986 "Tailor-Made Multi-Scale Materials Systems" Project number 192346071).

Declarations

Conflicts of Interest
The authors declare that they have no known competing financial interest or other interests that might be perceived to influence the results and/or discussion reported in this paper.

Additional information
Correspondence and requests for materials should be addressed to Y.S.

Reprints and permissions information is available at www.nature.com/reprints.

Publisher's note Springer Nature remains neutral with regard to jurisdictional claims in published maps and institutional affiliations.